

RESEARCH LETTER

10.1029/2018GL078604

Key Points:

- Strong electromagnetic ion cyclotron (EMIC) waves were observed during a non-storm time electron dropout event
- Simultaneous particle precipitation was observed for >30 keV protons and energetic electrons in a broad energy range (>~30 keV)
- Quasi-linear theory shows that EMIC waves dominate precipitation of high-energy electrons but underestimates low-energy electron precipitation

Correspondence to:

W. Li,
wenli77@bu.edu

Citation:

Capannolo, L., Li, W., Ma, Q., Zhang, X.-J., Redmon, R. J., Rodriguez, J. V., et al. (2018). Understanding the driver of energetic electron precipitation using coordinated multisatellite measurements. *Geophysical Research Letters*, 45, 6755–6765. <https://doi.org/10.1029/2018GL078604>

Received 4 MAY 2018

Accepted 29 JUN 2018

Accepted article online 5 JUL 2018

Published online 19 JUL 2018

Understanding the Driver of Energetic Electron Precipitation Using Coordinated Multisatellite Measurements

L. Capannolo¹ , W. Li¹ , Q. Ma^{1,2} , X.-J. Zhang^{2,3} , R. J. Redmon⁴ , J. V. Rodriguez⁴ , C. A. Kletzing⁵ , W. S. Kurth⁵ , G. B. Hospodarsky⁵ , M. J. Engebretson⁶ , H. E. Spence⁷ , and G. D. Reeves⁸ 

¹Center for Space Physics, Boston University, Boston, MA, USA, ²Department of Atmospheric and Oceanic Sciences, University of California, Los Angeles, CA, USA, ³Department of Earth, Planetary, and Space Sciences, University of California, Los Angeles, CA, USA, ⁴National Centers for Environmental Information, NOAA, Boulder, CO, USA, ⁵Department of Physics and Astronomy, University of Iowa, Iowa City, IA, USA, ⁶Department of Physics, Augsburg University, Minneapolis, MN, USA, ⁷Institute for the Study of Earth, Oceans, and Space, University of New Hampshire, Durham, NH, USA, ⁸Space Science and Applications Group, Los Alamos National Laboratory, Los Alamos, NM, USA

Abstract Magnetospheric plasma waves play a significant role in ring current and radiation belt dynamics, leading to pitch angle scattering loss and/or stochastic acceleration of the particles. During a non-storm time dropout event on 24 September 2013, intense electromagnetic ion cyclotron (EMIC) waves were detected by Van Allen Probe A (Radiation Belt Storm Probes-A). We quantitatively analyze a conjunction event when Van Allen Probe A was located approximately along the same magnetic field line as MetOp-01, which detected simultaneous precipitation of >30 keV protons and energetic electrons over an unexpectedly broad energy range (>~30 keV). Multipoint observations together with quasi-linear theory provide direct evidence that the observed electron precipitation at higher energy (>~700 keV) is primarily driven by EMIC waves. However, the newly observed feature of the simultaneous electron precipitation extending down to ~30 keV is not supported by existing theories and raises an interesting question on whether EMIC waves can scatter such low-energy electrons.

Plain Language Summary Energetic electrons can move from the magnetosphere into the Earth's upper atmosphere and cause chemical changes in the atmosphere leading to ozone reduction. The present paper studies the physical process that causes such electron precipitation. When a charged particle interacts with a plasma wave, its trajectory can be altered such that the particle falls into the upper atmosphere, but this process occurs only for a specific range of particle energy. In this study, we use one satellite (MetOp-01) orbiting in the upper atmosphere (altitude ~800 km) that can detect particle precipitation, and a Van Allen Probes satellite, which provides wave measurements in the equatorial magnetosphere. During the electron precipitation detected by MetOp-01, a Van Allen Probes satellite observed strong electromagnetic ion cyclotron (EMIC) waves. Multipoint satellite observations together with quasi-linear theory provide a direct evidence that the observed electron precipitation is primarily driven by EMIC waves. Another new interesting finding is that the precipitation occurs not only for electrons at high energies (>~1 MeV) but also at low energies (down to ~30 keV). This newly observed feature is not supported by existing theories and raises an interesting question whether EMIC waves can interact with such low-energy electrons as well.

1. Introduction

The relativistic electrons that populate the outer radiation belt are characterized by significant flux variations due to the complex balance between transport, loss, and acceleration processes, especially during enhanced geomagnetic activity (Reeves et al., 2003). The interaction between magnetospheric plasma waves and charged particles, which results in particle acceleration or loss, strongly affects the ring current and radiation belt dynamics (Thorne, 2010). The relativistic electrons that populate the highly dynamic outer radiation belt can be lost mainly due to magnetopause shadowing and the subsequent outward radial diffusion (Shprits et al., 2006; Turner et al., 2012), or efficient precipitation into the upper atmosphere caused by electromagnetic ion cyclotron (EMIC) waves and other wave modes through pitch angle scattering into the loss cone (W. Li et al., 2007; Shprits et al., 2017; Summers & Thorne, 2003; Thorne, 2010; Usanova et al., 2014).

EMIC waves are electromagnetic waves that typically occur in three distinct frequency bands below the gyrofrequencies of hydrogen (f_{cH}), helium (f_{cHe}), and oxygen (f_{cO}) (Erlandson & Ukhorskiy, 2001; Fraser et al., 2010).

EMIC waves are excited by the injection of anisotropic hot ring current ions from the plasmashet (Jordanova et al., 2008) and are therefore more likely to be associated with enhanced geomagnetic activity (Fraser et al., 2010). This excitation is more efficient in the overlap region of ring current ions and plasmasphere (Chen et al., 2010; Pickett et al., 2010) and in dayside plumes (Morley et al., 2010).

Many studies have reported EMIC wave observations both in space (Anderson et al., 1992; Erlandson & Ukhorskiy, 2001; Z. Li et al., 2014; Meredith et al., 2014; Min et al., 2012; Saikin et al., 2015; Zhang et al., 2011) and at the ground (Engebretson et al., 2008; Usanova et al., 2008) in the Pc1 and Pc2 bands. H-band EMIC waves dominate in the dawn sector, while He-band EMIC waves occur more frequently in the dusk sector (Min et al., 2012) but can span a broad magnetic local time (MLT) range for very intense EMIC waves (Tetrick et al., 2017). Dayside EMIC waves are more spatially extended, while nightside EMIC waves tend to be more localized and persistent, suggesting different generation mechanisms (Blum et al., 2017).

The EMIC waves interact with protons and electrons via cyclotron resonance and are more efficient in pitch angle scattering than energy diffusion for electrons (Summers et al., 1998). Ring current protons with energies of tens of keV can be scattered into the loss cone (Cao et al., 2016; Summers et al., 2017; Xiao et al., 2011) and produce proton aurora (Miyoshi et al., 2008; Yuan et al., 2010). The minimum energy (E_{\min}) of electrons resonating with EMIC waves depends strongly on various parameters, such as wave frequency spectrum, plasma density, and ion composition (W. Li et al., 2007; Meredith et al., 2014; Summers & Thorne, 2003). Precipitation of radiation belt electrons into the atmosphere due to resonant scattering has been observed at relativistic energies (>1 MeV) (Z. Li et al., 2014; Zhang et al., 2016). More recently, Hendry et al. (2017) reported that the dominant energy of the peak precipitating electron flux in association with EMIC waves is ~ 300 keV, and only $\sim 11\%$ of the precipitation events have the peak energy >1 MeV. Nonresonant scattering due to EMIC waves is suggested to potentially lower E_{\min} to a few hundred keV (Chen et al., 2016). However, further investigation is necessary to fully understand the E_{\min} of electrons, which can be potentially precipitated into the upper atmosphere.

Despite past studies of energetic electron precipitation, direct evidence of electron precipitation driven by EMIC waves as well as the associated energy of precipitating electrons is still lacking. An efficient method is to combine measurements of EMIC waves in the radiation belt with electron precipitation in the upper atmosphere during magnetic conjunction events, as shown in previous works (Blum et al., 2015; Clilverd et al., 2015; Z. Li et al., 2014; Miyoshi et al., 2008; Rodger et al., 2015). In the present study, we focus on analyzing the role of various magnetospheric waves in energetic electron precipitation during an interesting conjunction event. This event is a non-storm time dropout “challenge” event, selected by the Geospace Environmental Modeling focus group “Quantitative Assessment of Radiation Belt Modeling”.

2. Satellite Data

For the equatorial measurements, we use the twin Van Allen Probes (Radiation Belt Storm Probes, RBSP). RBSP-A and RBSP-B both have orbital periods of 9 hr, a perigee of ~ 600 km and apogee of $\sim 6 R_E$ (Mauk et al., 2013). We use the wave measurements from Electric and Magnetic Field Instrument Suite and Integrated Science (EMFISIS; Kletzing et al., 2013) to analyze magnetospheric wave properties. The triaxial fluxgate magnetometer measures the vector magnetic field and low frequency waves below 30 Hz. Plasma density is inferred from the upper hybrid resonance frequency detected by EMFISIS (Kurth et al., 2015). Particle fluxes from the Energetic Particle, Composition, and Thermal Plasma Suite (ECT; Spence et al., 2013) are used to analyze the pitch angle and energy distributions of protons and electrons.

For the low altitude observations, we use the NOAA Polar Operational Environmental Satellites (POES) and European Organisation for the Exploitation of Meteorological Satellites (EUMETSAT) MetOp satellite network (Evans & Greer, 2004). These multiple spacecraft have altitudes of 800–850 km and periods of ~ 100 min, covering different MLT sectors. Electron and proton fluxes are measured in different energy channels by the Medium Energy Proton and Electron Detector (MEPED). In this study, we use the proton channel P1 (~ 30 – 80 keV) and the electron energy channels E1 (>30 keV), E2 (>100 keV), E3 (>300 keV), and E4 (>700 keV). E4 is a virtual channel obtained from the proton channel P6 (>6.9 MeV), which is contaminated mainly by electrons above ~ 700 – 800 keV (Carson et al., 2013; Green, 2013; Rodger et al., 2010; Yando et al., 2011). The E4 channel is more sensitive to relativistic electrons, given its effective energy at ~ 879 keV (Peck et al., 2015). At high latitudes, POES and MetOp satellites provide measurements

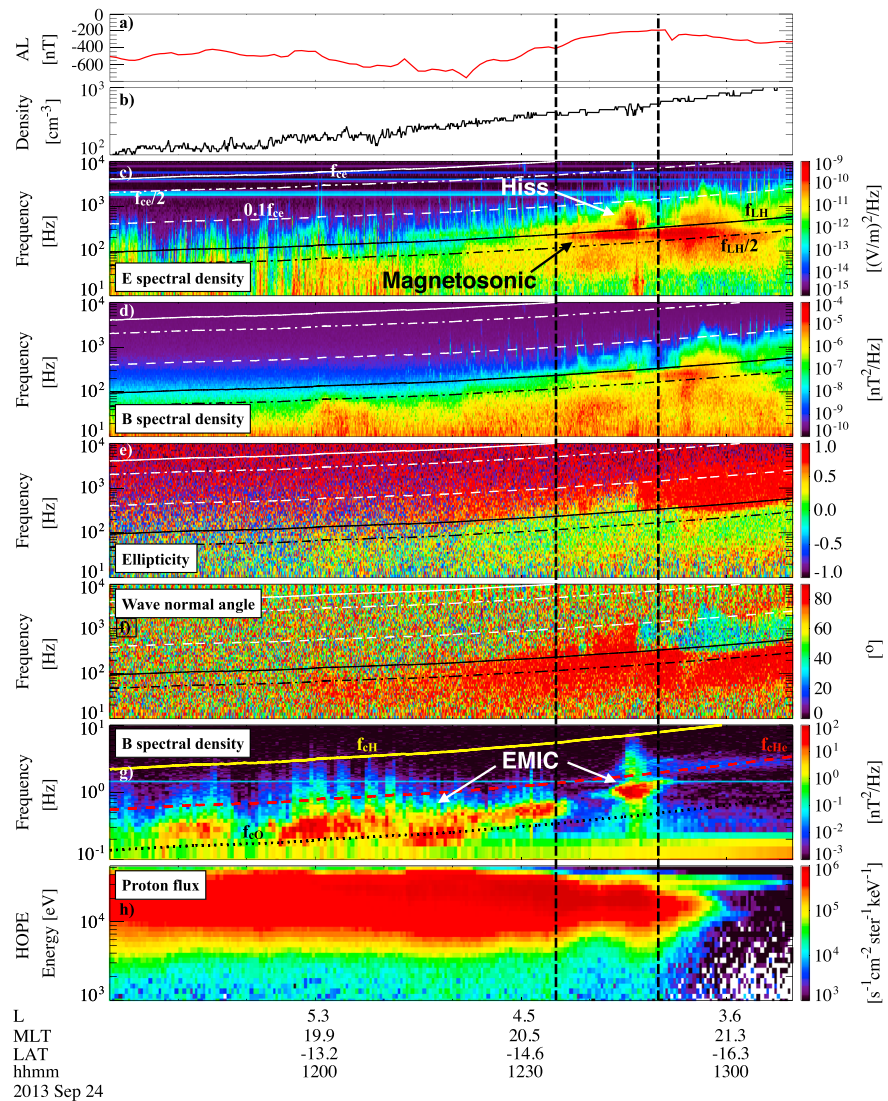


Figure 1. RBSP-A observations during 11:30–13:10 UT on 24 September 2013. (a) Kyoto AL index, (b) plasma density, (c) electric and (d) magnetic power spectral density, (e) ellipticity and (f) wave normal angle, (g) EMIC wave magnetic power spectral density, and (h) proton flux measured by the HOPE (Helium, Oxygen, Proton, Electron) mass spectrometer (Funsten et al., 2013). The black dashed lines indicate the L-shell span 4.3–3.9 of RBSP-A during magnetic conjunction with MetOp-01. The white lines represent the electron gyrofrequency (f_{ce} ; solid), $0.5f_{ce}$ (dash dotted), and $0.1f_{ce}$ (dashed). The black lines indicate the lower hybrid resonance frequency (f_{LH} ; solid) and $0.5f_{LH}$ (dash dotted). The yellow solid line corresponds to f_{cH} , the dashed red line is the He+ gyrofrequency (f_{cHe}), and the black dotted line is the O+ gyrofrequency (f_{cO}).

approximately along the magnetic field line (0° telescope) and perpendicular to it (90° telescope), allowing us to distinguish precipitating particles from trapped ones. Proton contamination in E1–E3 was removed using the methods described in Peck et al. (2015) and corrected electron count rates are converted to fluxes through the geometric factors in Table 3–2 in Green (2013).

3. Observations

Figure 1 shows the wave and particle dynamics measured by RBSP-A during a non-storm time event, when Dst remained above -30 nT during the entire day of 24 September 2013 (not shown). From $\sim 11:30$ UT to $\sim 13:00$ UT, the plasma density remained above 100 cm^{-3} (Figure 1b), suggesting that RBSP-A was inside the plasmasphere. Based on the wave power spectra (Figures 1c and 1d) together with wave ellipticity (Figure 1e) and wave normal angle (Figure 1f), plasmaspheric hiss and magnetosonic waves were found to be present, particularly after $\sim 12:30$ UT. In association with substorm activity, RBSP-A observed persistent

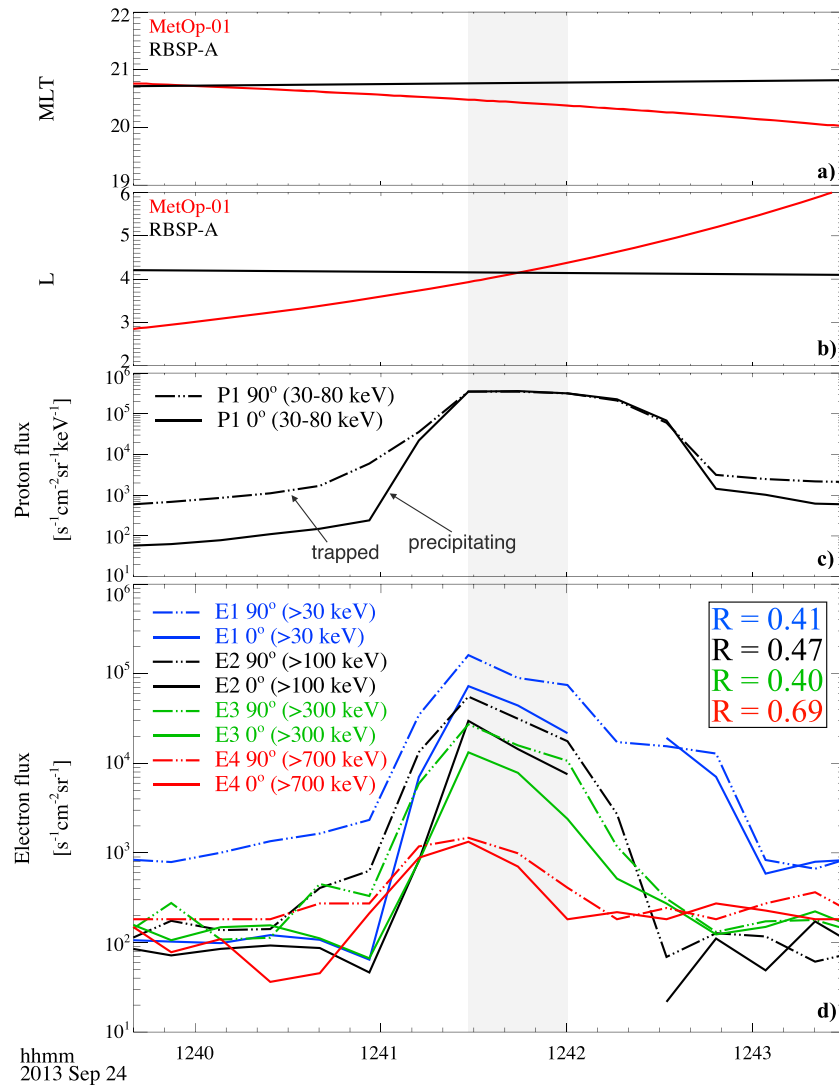


Figure 2. MetOp-01 observations during the magnetic conjunction with RBSP-A. (a) MLT and (b) L shell for RBSP-A (black) and MetOp-01 (red); (c) proton flux at $\sim 30\text{--}80$ keV; and (d) electron flux for the energy channels >30 keV (blue), >100 keV (black), >300 keV (green), and >700 keV (red), after removing proton contamination. Double-dot dashed lines are measurements from the 90° -pointing telescope, indicative of trapped particles; solid lines are from the 0° -pointing telescope, indicative of precipitating particles. The boxed legend in (d) shows the ratio (R) of precipitating and trapped particle fluxes averaged over the gray shaded region color coded for different electron energy channels.

EMIC wave activity from 11:30 UT to 13:00 UT (over the L-shell from ~ 3.8 to ~ 5.6 and the MLT from ~ 19.5 to ~ 21.2), mostly in the Helium band, but also partially crossing the helium and oxygen gyrofrequencies (Figure 1g). The EMIC wave intensity was associated with the proton flux modulation (Figure 1h), especially for the very isolated EMIC waves over 12:35–12:50 UT (Figures 1g and 1h).

We take advantage of the magnetic conjunction between RBSP-A and MetOp-01 (operationally, MetOp-B) occurring during this isolated EMIC wave activity around 12:45 UT, at $L \sim 4.1$ and $MLT \sim 20.7$. During the conjunction period (highlighted by the dashed black lines in Figure 1), EMIC wave activity was strongest in the He-band (root-mean-square wave amplitude $B_w > 5$ nT) but also exhibited modest wave power in the H-band ($B_w \sim 0.7$ nT). Although plasmaspheric hiss and magnetosonic waves were also present, the wave amplitudes (~ 6 and ~ 24 pT, respectively) were much weaker than those of the observed EMIC waves. The plasma density inferred from the upper hybrid resonance line detected by EMFISIS was 492 cm^{-3} near the conjunction period.

The MetOp-01 observations during the conjunction with RBSP-A are shown in Figure 2. The two satellites were in a very close magnetic conjunction, with differences less than ± 0.5 in L-shell and ± 0.5 hr in MLT

(Figures 2a and 2b) between 12:40 UT and 12:43 UT. Figures 2c and 2d show the observed proton and electron fluxes in different energy channels. The fluxes from both the 0° and 90° telescopes are shown, respectively, corresponding to precipitating (solid lines) and trapped (double-dot-dashed lines) particles. The data shown in Figure 2 were averaged over 16 s from the full 2-s resolution to show the overall trend more clearly.

During the conjunction period, simultaneous precipitation of tens of keV protons and electrons at all four energy channels (from $>\sim 30$ keV to $>\sim 700$ keV) were observed, as highlighted by the gray shaded area in Figure 2. The 30–80 keV proton flux measured by the 0° telescope increased sharply at 12:41:10 UT, and reached close to the flux of trapped protons for ~ 90 s. Simultaneously, the flux of precipitating electrons at energies $>\sim 700$ keV (solid red line in Figure 2d) increased and almost approached the value of trapped electrons. Although electron precipitation also occurred in energy channels at $>\sim 30$, $>\sim 100$, and $>\sim 300$ keV, the flux of precipitating electrons is noticeably lower than that of the trapped electrons. To quantify the level of precipitation, the ratios of precipitating-to-trapped particle fluxes ($R = J_0/J_{90}$) were calculated by averaging over the gray shaded area and marked in Figure 2d, color-coded for each energy channel. The ratio is larger for $>\sim 700$ keV electrons ($R = 0.69$), compared to the value for $<\sim 700$ keV electrons ($R \sim 0.4$). Note that although the R value for $>\sim 700$ keV electrons appeared to remain close to 1 throughout the majority of the plotted time interval, the R value before 12:41 UT and after 12:42 UT may not be reliable, since both precipitating and trapped fluxes remained low, probably close to the background. It is worthwhile to note that particle precipitation extended to higher L-shells (up to ~ 5) even after the conjunction period ($\sim 12:42$ UT), especially for 30–80 keV protons. This is consistent with the RBSP-A observation in Figure 1g, where EMIC waves were also detected over an extensive region (L-shells from ~ 3.8 to ~ 5.6). Within the time interval of the observed EMIC wave activity, the simultaneous precipitation of 30–80 keV protons and electrons at all four energy channels (from $>\sim 30$ to $>\sim 700$ keV) was also detected by NOAA-16 at $\sim 11:32$ UT (MLT ~ 19.4 , $L \sim 4.6$, not shown) and MetOp-02 at $\sim 11:47$ UT (MLT ~ 20.1 , $L \sim 4.4$, not shown), although the conjunction with RBSP was not very tight (with an L-shell difference of ~ 1.5). In the present paper, we focus on the tight RBSP-A/MetOp-01 conjunction, which allows us to quantify energetic electron precipitation driven by magnetospheric waves observed near the conjugate magnetic equator.

To evaluate the effect of EMIC wave activity on electron dynamics, we calculate the phase space density (PSD) for the fixed first (μ) and second (K) adiabatic invariants (Chen et al., 2006), based on the measured electron fluxes from both Van Allen Probes. Figure 3 shows the evolution of PSD as a function of L^* calculated based on the TS04D model (Tsyganenko & Sitnov, 2005), for different combinations of μ and K , from 08:00 UT (before the EMIC waves were detected) to 16:00 UT (well after EMIC wave detection). The color-coded lines follow the trajectories of Van Allen Probes A and B. Note that the EMIC wave activity during the conjunction was observed at $L^* \sim 3.8$ ($L \sim 4.1$), highlighted by a gray shaded area in each panel. Interestingly, the PSD profiles before (10:00 UT) and after (13:00 UT) EMIC wave observations show different features around $L^* \sim 3.8$, depending on the values of μ and K . For $\mu = 800$ MeV/G (electron energies ~ 1.5 – 3 MeV at $L^* \sim 3.8$), the PSD exhibits little changes at $K = 0.05$ $G^{0.5}$ R_E (Figure 3b), but the PSD decrease tends to be more evident at larger K (Figures 3e and 3h). Compared to $\mu = 800$ MeV/G, electron PSD at $\mu = 2,000$ MeV/G (electron energies ~ 3 – 5 MeV at $L^* \sim 3.8$) exhibits a more significant decrease across all K values. Such localized PSD dips with μ and K dependence are unlikely related to magnetopause shadowing together with outward radial diffusion, but clear signatures of local pitch angle scattering loss, possibly driven by EMIC wave activity (Xiang et al., 2017). EMIC waves are indeed found to be more efficient in scattering higher energy ($>\sim$ MeV) electrons with low-intermediate pitch angles (Jordanova et al., 2008; Kersten et al., 2014; Meredith et al., 2003; Usanova et al., 2014). Note that the localized PSD dips were extended to a broad region up to $L^* \sim 5$, which is consistent with EMIC wave activity observed over a wide range of L-shells (from ~ 3.8 to ~ 5.6), as shown in Figure 1g. These results are in agreement with previous studies of the same dropout event (Su et al., 2016) and other case studies as well (Shprits et al., 2017; Zhang et al., 2016).

For low μ (Figures 3a, 3d, and 3g), however, the PSD profile following the EMIC wave detection slightly increases for low K . Such feature is consistent with an ongoing injection of electrons at energies below a few hundred keV, also observed by the geosynchronous GOES-15 spacecraft during ~ 10 – 15 UT (not shown) in the postmidnight sector. Injection and acceleration of electrons are more efficient for electrons at pitch angles closer to 90°, as supported by a larger PSD increase at $K = 0.05$ $G^{0.5}$ R_E (corresponding to pitch angles of $\sim 70^\circ$) than that at $K \geq 0.2$ $G^{0.5}$ R_E (corresponding to pitch angles below $\sim 50^\circ$).

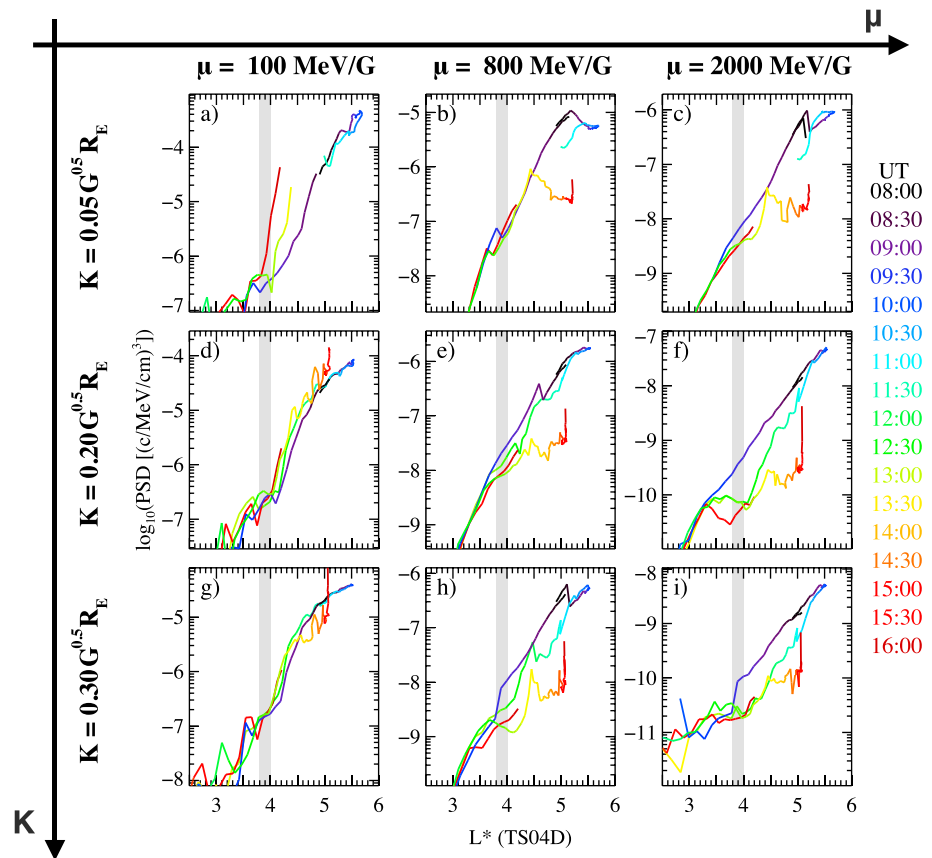


Figure 3. The evolution of electron PSD as a function of L^* based on the TS04D model by Tsyganenko and Sitnov (2005) over 08:00–16:00 UT on 24 September 2013, color coded in UT, for different combinations of μ and K . Constant values of μ are sorted in columns (from the left: 100, 800, and 2,000 MeV/G) and constant values of K are shown in rows (from the top: $0.05 G^{0.5} R_E$, $0.20 G^{0.5} R_E$, and $0.30 G^{0.5} R_E$). The gray shaded regions indicate $L^* \sim 3.8$, where the magnetic conjunction occurred.

4. Theoretical Estimates of Electron Pitch Angle Scattering

Using quasi-linear theory (Ni et al., 2015; Summers, 2005), we calculate the pitch angle scattering rate of the observed waves during this conjunction event. Figure 4 shows the bounce-averaged pitch angle diffusion coefficients due to the EMIC waves (Figure 4a: He-band; Figure 4b: H-band), plasmaspheric hiss (Figure 4c), and magnetosonic (Figure 4d) waves. The diffusion coefficients are calculated based on the wave and plasma parameters measured by RBSP-A between 12:44 and 12:48 UT, when the intense EMIC waves were observed near the conjunction period. The wave frequency spectra were obtained from the satellite measurements with the lower (upper) cutoff frequencies of $0.26 f_{cH}$ ($0.99 f_{cH}$) for H-band EMIC waves and $0.26 f_{cHe}$ ($0.99 f_{cHe}$) for He-band EMIC waves, respectively. We assume wave normal angles change from quasi-parallel near the equator to more oblique up to 40° in latitude, following the latitudinally varying wave normal angle model in Ni et al. (2015). The cold ion composition is assumed to be 70% H^+ , 20% He^+ , and 10% O^+ (Lee & Angelopoulos, 2014; Meredith et al., 2014), while the resonance numbers considered in the calculation are between -5 and 5 , including Landau resonance. The ratio of plasma frequency to electron cyclotron frequency (f_{pe}/f_{ce}), calculated based on the observation, is ~ 15.3 .

Given the high EMIC wave amplitude, the pitch angle diffusion coefficients due to EMIC waves (Figures 4a and 4b) are much larger than those driven by plasmaspheric hiss (Figure 4c) or magnetosonic waves (Figure 4d). More specifically, pitch angle diffusion coefficients of He-band EMIC waves (Figure 4a) are typically stronger than those of H-band (Figure 4b), particularly at energies above several hundred keV. He-band EMIC waves can scatter electrons above ~ 300 keV but are most efficient for electrons above 3 MeV, on a time-scale of $< \sim 10$ min. Interestingly, the minimum resonant energy of electrons that can be scattered by EMIC

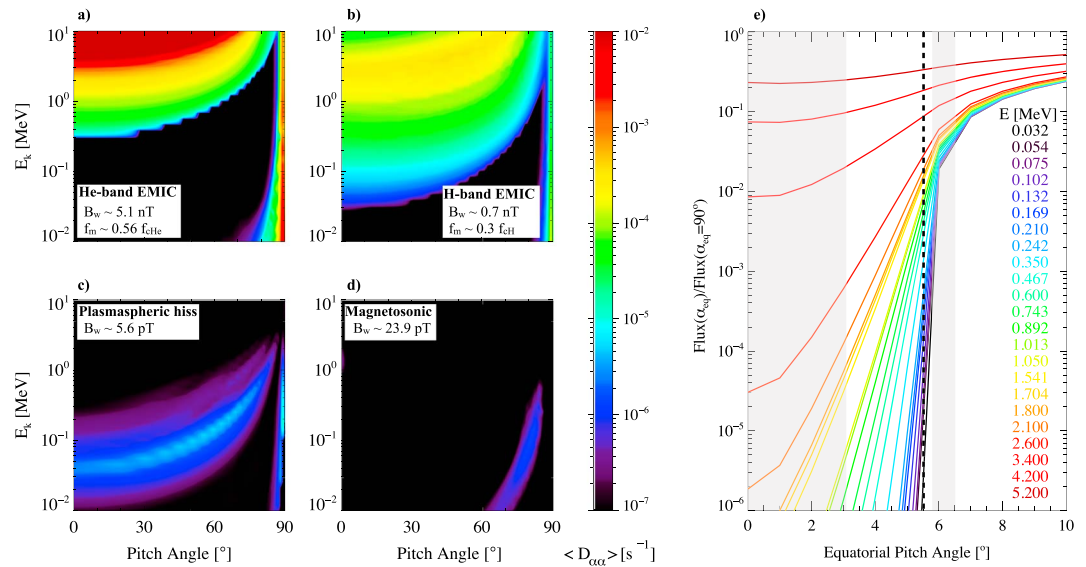


Figure 4. (a–d) Bounce-averaged diffusion coefficients as a function of equatorial pitch angle and kinetic energy E_k for the observed waves (amplitude B_w , central frequency f_m). Ion composition is assumed to be 70% H^+ , 20% He^+ , and 10% O^+ (Lee & Angelopoulos, 2014). Ratio of plasma frequency to electron cyclotron frequency (f_{pe}/f_{ce}) is ~ 15.3 . (e) Electron flux normalized to that at 90° pitch angle as a function of equatorial pitch angle, color coded by energy (MeV). The dashed line indicates the equatorial bounce loss cone angle at $L \sim 4$. The gray shaded regions represent the mapped range of the equatorial pitch angles corresponding to the local pitch angles measured by the 0° (left) and 90° (right) telescopes onboard MetOp-01.

waves extends to lower energy (tens of keV) for the H-band, although the scattering rate is much lower than that at higher energies. In agreement with previous results (Kersten et al., 2014; Usanova et al., 2014; Zhang et al., 2016), EMIC waves propagating quasi-parallel to the magnetic field are effective in scattering electrons at low-intermediate pitch angles depending on energy. The EMIC waves can also cause the electron scattering around 90° pitch angle via Landau resonance, but the loss of high pitch angle electrons is inefficient due to the lack of scattering at intermediate pitch angles. The pitch angle diffusion coefficients due to plasmaspheric hiss (Figure 4c) and magnetosonic waves (Figure 4d) are much weaker than those caused by EMIC waves, indicating that these waves play a minor role in electron precipitation in this dropout event.

To quantify the precipitation of electrons due to the observed waves, we use the total diffusion coefficients (caused by EMIC, hiss, and magnetosonic waves) to estimate the normalized equatorial electron pitch angle distribution after reaching a quasi-equilibrium state (formulae by Theodoridis & Paolini, 1967; W. Li et al., 2013), during which process the electron flux decays exponentially due to pitch angle scattering loss (Ni et al., 2013; O'Brien et al., 2014), while maintaining its shape as a function of pitch angle. Figure 4e shows the electron flux normalized to that at 90° equatorial pitch angle as a function of equatorial pitch angle, color coded by energy. The equatorial bounce loss cone angle at $L \sim 4$ is marked by a black dashed vertical line. The gray shaded regions represent approximately the ranges of equatorial pitch angles corresponding to the local pitch angles of electrons detected by the 0° and 90° telescopes onboard MetOp-01, considering the telescope field of view of 15° . The loss cone becomes more filled as energy increases, showing that EMIC waves are indeed more efficient in scattering electrons into the loss cone at higher energy. More specifically, pitch angle scattering reaches the strong diffusion limit (R close to 1) at energies above several MeV. However, the estimated ratios are much smaller than 0.1 for electrons below ~ 1 MeV and 0.1–0.7 for electrons above a few MeV. These estimated R values are much smaller than those inferred from the MetOp-01 measurements in Figure 2d at low energies (below ~ 1 MeV) but become comparable at high energies (above a few MeV). Note that the direct quantitative comparison between the measured and estimated ratio is difficult, since the electron fluxes measured by POES were integrated over a broad energy range. Nevertheless, the trend of a higher ratio of precipitating-to-trapped electron fluxes at higher energies ($> \sim 700$ keV) and a lower ratio at lower energies ($< \sim 700$ keV) is overall consistent with the MetOp-01 observations (Figure 2d), which clearly

shows the highest ratio in the E4 channel (red lines, $R = 0.69$) compared to the ratios at lower energy channels (blue, black, and green lines, $R \sim 0.4$).

5. Summary and Discussion

We quantitatively analyzed a magnetic conjunction event between RBSP-A and MetOp-01, which occurred on 24 September 2013.

During the conjunction, RBSP-A detected strong EMIC waves inside the plasmasphere at $L \sim 4.1$ ($L^* \sim 3.8$) and $MLT \sim 20.7$, and MetOp-01 observed the simultaneous precipitation of $> \sim 30$ keV protons, and energetic electrons from $> \sim 30$ to $> \sim 700$ keV at the conjugate low altitude. The observed EMIC waves were strongest in the He band ($B_w \sim 5.1$ nT) but also extended to the H band with a lower amplitude ($B_w \sim 0.7$ nT). Although plasmaspheric hiss and magnetosonic waves were present, their intensities were much weaker than those of EMIC waves.

The electron PSD evolution for this event shows that the electron loss was clearly localized over L^* from ~ 3.8 to ~ 5 , mainly affecting high-energy electrons ($> \sim 1.5$ MeV). This is consistent with the EMIC wave activity, which was also observed in a similar radial extent. The observed localized PSD dips are inconsistent with electron losses due to magnetopause shadowing and the subsequent outward radial diffusion but support electron loss through local pitch angle scattering primarily driven by EMIC waves at $L > \sim 4$ (Su et al., 2016). Although MetOp-01 detected electron precipitation as low as ~ 30 keV, the PSD evolution based on the RBSP-A measurement did not exhibit such loss below several hundred keV energies. These magnetospheric observations might suggest that electron injection, associated with substorm activity (Turner et al., 2015), dominates over the loss at such low energies, leading to a net small increase in electron PSD. These PSD increases were observed only for low values of $K (< 0.20 G^{0.5} R_E)$, in agreement with substorm injection, which is more efficient for electrons at pitch angles closer to 90° .

We estimate the electron precipitation driven by EMIC waves, plasmaspheric hiss, and magnetosonic waves using quasi-linear theory based on the observed wave and plasma parameters and show that EMIC waves are efficient in scattering electrons only at low-intermediate pitch angles. In particular, He-band EMIC waves are mainly responsible for providing strong pitch angle scattering for highly relativistic electrons (greater than a few MeV) on a timescale of ~ 10 min, while H-band EMIC waves can scatter electrons into the loss cone at lower energies (down to tens of keV) but on a much longer timescale (\sim day). The plasmaspheric hiss and magnetosonic waves play minor roles in electron precipitation in this dropout event primarily due to their much weaker intensity. The comparison between the observed and estimated ratio of precipitating-to-trapped electron fluxes demonstrates that the trend of estimated ratios (larger ratio at larger energy $> \sim 700$ keV compared to lower energy $< \sim 700$ keV) primarily due to EMIC waves is overall consistent with observations. However, the pitch angle scattering rates calculated based on the quasi-linear theory significantly underestimate electron precipitation at energies less than a few MeV. This may suggest that quasi-linear theory cannot explain the EMIC-driven electron precipitation at lower energies.

The minimum energy of electrons that can be scattered by EMIC waves is previously believed to remain above ~ 1 MeV (Kersten et al., 2014; Meredith et al., 2003). However, recent observations reported the potential presence of much lower minimum energy (approximately hundreds of keV) of electrons subject to EMIC-driven pitch angle scattering (Clilverd et al., 2015; Hendry et al., 2017; Rodger et al., 2015; Yahnin et al., 2016, 2017). Our study newly reports a very interesting event, where the minimum energy of precipitating electrons can potentially extend to unexpectedly low energy ($> \sim 30$ keV), in association with strong EMIC waves without the presence of any other magnetospheric waves effective in electron precipitation. Although the recently proposed nonresonant interaction due to the spatial sharp edge associated with EMIC wave packets may potentially explain the electron precipitation down to few hundred keV (Chen et al., 2016), it may still be difficult to explain the electron precipitation down to ~ 30 keV. Our new finding offers credible insights into understanding the interactions between the EMIC waves and energetic electrons. It will be interesting to investigate how often EMIC waves are associated with electron precipitation with energies extending down to ~ 30 keV, but it is beyond the scope of this pilot study and remains as future work. Although further investigations of multievent analysis, theory, and modeling are needed to fully understand the precipitation of lower energy electrons, our study provides a new direct evidence of highly energetic electron precipitation driven by EMIC waves using a fortuitous magnetic conjunction between RBSP-A and MetOp-01.

Acknowledgments

This research is supported by NSF grant AGS-1723588, AFOSR grant FA9550-15-1-0158, and the Alfred P. Sloan Research Fellowship grant FG-2018-10936. Work at Augsburg University was supported by NSF grants PLR-1341493 and AGS-1651263. Work at UNH was supported by NASA grant NNX15AF66G and NASA Contract NAS5-01072. The research at the University of Iowa was supported by JHU/APL contract 921647 under NASA Prime contract NAS5-01072. We acknowledge the GEM focus group of "Quantitative Assessment of Radiation Belt Modeling" for coordinating the efforts from the community to provide helpful resources during "Challenge" events. The Van Allen Probes data from the EMFISIS instrument were obtained from <http://emfisis.physics.uiowa.edu/Flight/>, and data from the ECT instrument were obtained from http://www.rbsp-ect.lanl.gov/dat_pub/. The POES and MetOp data were obtained from <https://www.ngdc.noaa.gov/stp/satellite/poes/>. We acknowledge the World Data Center for Geomagnetism, Kyoto, for providing AE, AL, and Dst indices (<http://wdc.kugi.kyoto-u.ac.jp/kp/index.html>).

References

- Anderson, B. J., Erlandson, R. E., & Zanetti, L. J. (1992). A statistical study of Pc 1–2 magnetic pulsations in the equatorial magnetosphere: 2. Wave properties. *Journal of Geophysical Research*, *97*, 3089–3101. <https://doi.org/10.1029/91JA02697>
- Blum, L. W., Bonnell, J. W., Agapitov, O., Paulson, K., & Kletzing, C. (2017). EMIC wave scale size in the inner magnetosphere: Observations from the dual Van Allen Probes. *Geophysical Research Letters*, *44*, 1227–1233. <https://doi.org/10.1002/2016GL072316>
- Blum, L. W., Halford, A., Millan, R., Bonnell, J. W., Goldstein, J., Usanova, M., et al. (2015). Observations of coincident EMIC wave activity and duskside energetic electron precipitation on 18–19 January 2013. *Geophysical Research Letters*, *42*, 5727–5735. <https://doi.org/10.1002/2015GL065245>
- Cao, X., Ni, B., Liang, J., Xiang, Z., Wang, Q., Shi, R., et al. (2016). Resonant scattering of central plasma sheet protons by multiband EMIC waves and resultant proton loss timescales. *Journal of Geophysical Research: Space Physics*, *121*, 1219–1232. <https://doi.org/10.1002/2015JA021933>
- Carson, B. R., Rodger, C. J., & Clilverd, M. A. (2013). POES satellite observations of EMIC-wave driven relativistic electron precipitation during 1998–2010. *Journal of Geophysical Research*, *118*, 232–243. <https://doi.org/10.1029/2012JA017998>
- Chen, L., Thorne, R. M., Bortnik, J., & Zhang, X.-J. (2016). Nonresonant interactions of electromagnetic ion cyclotron waves with relativistic electrons. *Journal of Geophysical Research: Space Physics*, *121*, 9913–9925. <https://doi.org/10.1002/2016JA022813>
- Chen, L., Thorne, R. M., Jordanova, V. K., Wang, C.-P., Gkioulidou, M., Lyons, L., & Horne, R. B. (2010). Global simulation of EMIC wave excitation during the 21 April 2001 storm from coupled RCM-RAM-HOTRAY modeling. *Journal of Geophysical Research*, *115*, A07209. <https://doi.org/10.1029/2009JA015075>
- Chen, Y., Friedel, R. H. W., & Reeves, G. D. (2006). Phase space density distributions of energetic electrons in the outer radiation belt during two Geospace Environment Modeling Inner Magnetosphere/Storms selected storms. *Journal of Geophysical Research*, *111*, A11504. <https://doi.org/10.1029/2006JA011703>
- Clilverd, M. A., Duthie, R., Hardman, R., Hendry, A. T., Rodger, C. J., Raita, T., et al. (2015). Electron precipitation from EMIC waves: A case study from 31 May 2013. *Journal of Geophysical Research: Space Physics*, *120*, 3618–3631. <https://doi.org/10.1002/2015JA021090>
- Engebretson, M. J., Lessard, M. R., Bortnik, J., Green, J. C., Horne, R. B., Detrick, D. L., et al. (2008). Pc1–Pc2 waves and energetic particle precipitation during and after magnetic storms: Superposed epoch analysis and case studies. *Journal of Geophysical Research*, *113*, A01211. <https://doi.org/10.1029/2007JA012362>
- Erlandson, R. E., & Ukhorskiy, A. J. (2001). Observations of electromagnetic ion cyclotron waves during geomagnetic storms: Wave occurrence and pitch angle scattering. *Journal of Geophysical Research*, *106*, 3883–3895. <https://doi.org/10.1029/2000JA000083>
- Evans, D. S., & Greer, M. S. (2004). Polar orbiting environmental satellite space environment monitor-2: Instrument descriptions and archive data documentation archive data documentation. *NOAA Tech. Mem.* 93, Version 1.4. Space Weather Predict. Cent., Boulder, Colo.
- Fraser, B. J., Grew, R. S., Morley, S. K., Green, J. C., Singer, H. J., Loto'aniu, T. M., & Thomsen, M. F. (2010). Storm time observations of electromagnetic ion cyclotron waves at geosynchronous orbit: GOES results. *Journal of Geophysical Research*, *115*, A05208. <https://doi.org/10.1029/2009JA014516>
- Funsten, H. O., Skoug, R. M., Guthrie, A. A., MacDonald, E. A., Baldonado, J. R., Harper, R. W., et al. (2013). Helium, Oxygen, Proton, and Electron (HOPE) mass spectrometer for the radiation belt storm probes mission. *Space Science Reviews*, *179*(1–4), 423–484. <https://doi.org/10.1007/s11214-013-9968-7>
- Green, J. C. (2013). MEPED telescope data processing algorithm theoretical basis document, Natl. Oceanic and Atmos. Admin. National Geophysical Data Center, Boulder, Colo.
- Hendry, A. T., Rodger, C. J., & Clilverd, M. A. (2017). Evidence of sub-MeV EMIC-driven electron precipitation. *Geophysical Research Letters*, *44*, 1210–1218. <https://doi.org/10.1002/2016GL071807>
- Jordanova, V. K., Albert, J., & Miyoshi, Y. (2008). Relativistic electron precipitation by EMIC waves from self-consistent global simulations. *Journal of Geophysical Research*, *113*, A00A10. <https://doi.org/10.1029/2008JA013239>
- Kersten, T., Horne, R. B., Glauert, S. A., Meredith, N. P., Fraser, B. J., & Grew, R. S. (2014). Electron losses from the radiation belts caused by EMIC waves. *Journal of Geophysical Research: Space Physics*, *119*, 8820–8837. <https://doi.org/10.1002/2014JA020366>
- Kletzing, C. A., Kurth, W. S., Acuna, M., MacDowall, R. J., Torbert, R. B., Averkamp, T., et al. (2013). The electric and magnetic field instrument suite and integrated science (EMFISIS) on RBSP. *Space Science Reviews*, *179*(1–4), 127–181. <https://doi.org/10.1007/s11214-013-9993-6>
- Kurth, W. S., De Pascuale, S., Faden, J. B., Kletzing, C. A., Hospodarsky, G. B., Thaller, S., & Wygant, J. R. (2015). Electron densities inferred from plasma wave spectra obtained by the waves instrument on Van Allen Probes. *Journal of Geophysical Research: Space Physics*, *120*, 904–914. <https://doi.org/10.1002/2014JA020857>
- Lee, J. H., & Angelopoulos, V. (2014). On the presence and properties of cold ions near Earth's equatorial magnetosphere. *Journal of Geophysical Research: Space Physics*, *119*, 1749–1770. <https://doi.org/10.1002/2013JA019305>
- Li, W., Ni, B., Thorne, R. M., Bortnik, J., Green, J. C., Kletzing, C. A., et al. (2013). Constructing the global distribution of chorus wave intensity using measurements of electrons by the POES satellites and waves by the Van Allen Probes. *Geophysical Research Letters*, *40*, 4526–4532. <https://doi.org/10.1002/grl.50920>
- Li, W., Shprits, Y. Y., & Thorne, R. M. (2007). Dynamic evolution of energetic outer zone electrons due to wave-particle interactions during storms. *Journal of Geophysical Research*, *112*, A10220. <https://doi.org/10.1029/2007JA012368>
- Li, Z., Millan, R. M., Hudson, M. K., Woodger, L. A., Smith, D. M., Chen, Y., et al. (2014). Investigation of EMIC wave scattering as the cause for the BARREL 17 January 2013 relativistic electron precipitation event: A quantitative comparison of simulation with observations. *Geophysical Research Letters*, *41*, 8722–8729. <https://doi.org/10.1002/2014GL062273>
- Mauk, B. H., Fox, N. J., Kanekal, S. G., Kessel, R. L., Sibeck, D. G., & Ukhorskiy, A. (2013). Science objectives and rationale for the Radiation Belt Storm Probes mission. *Space Science Reviews*, *179*(1–4), 3–27. <https://doi.org/10.1007/s11214-012-9908-y>
- Meredith, N. P., Horne, R. B., Kersten, T., Fraser, B. J., & Grew, R. S. (2014). Global morphology and spectral properties of EMIC waves derived from CRRES observations. *Journal of Geophysical Research: Space Physics*, *119*, 5328–5342. <https://doi.org/10.1002/2014JA020064>
- Meredith, N. P., Thorne, R. M., Horne, R. B., Summers, D., Fraser, B. J., & Anderson, R. R. (2003). Statistical analysis of relativistic electron energies for cyclotron resonance with EMIC waves observed on CRRES. *Journal of Geophysical Research*, *108*(A6), 1250. <https://doi.org/10.1029/2002JA009700>
- Min, K., Lee, J., Keika, K., & Li, W. (2012). Global distribution of EMIC waves derived from THEMIS observations. *Journal of Geophysical Research*, *117*, A05219. <https://doi.org/10.1029/2012JA017515>
- Miyoshi, Y., Sakaguchi, K., Shiokawa, K., Evans, D., Albert, J., Connors, M., & Jordanova, V. (2008). Precipitation of radiation belt electrons by EMIC waves, observed from ground and space. *Geophysical Research Letters*, *35*, L23101. <https://doi.org/10.1029/2008GL035727>
- Morley, S. K., Friedel, R. H. W., Cayton, T. E., & Noveroske, E. (2010). A rapid, global and prolonged electron radiation belt dropout observed with the global positioning system constellation. *Geophysical Research Letters*, *37*, L06102. <https://doi.org/10.1029/2010GL042772>

- Ni, B., Bortnik, J., Thorne, R. M., Ma, Q., & Chen, L. (2013). Resonant scattering and resultant pitch angle evolution of relativistic electrons by plasmaspheric hiss. *Journal of Geophysical Research: Space Physics*, *118*, 7740–7751. <https://doi.org/10.1002/2013JA019260>
- Ni, B., Cao, X., Zou, Z., Zhou, C., Gu, X., Bortnik, J., et al. (2015). Resonant scattering of outer zone relativistic electrons by multiband EMIC waves and resultant electron loss time scales. *Journal of Geophysical Research: Space Physics*, *120*, 7357–7373. <https://doi.org/10.1002/2015JA021466>
- O'Brien, T. P., Claudepierre, S. G., Blake, J. B., Fennell, J. F., Clemmons, J. H., Roeder, J. L., et al. (2014). An empirically observed pitch-angle diffusion eigenmode in the Earth's electron belt near $L^* = 5.0$. *Geophysical Research Letters*, *41*, 251–258. <https://doi.org/10.1002/2013GL058713>
- Peck, E. D., Randall, C. E., Green, J. C., Rodriguez, J. V., & Rodger, C. J. (2015). POES MEPED differential flux retrievals and electron channel contamination correction. *Journal of Geophysical Research: Space Physics*, *120*, 4596–4612. <https://doi.org/10.1002/2014JA020817>
- Pickett, J. S., Grison, B., Omura, Y., Engebretson, M. J., Dandouras, I., Masson, A., et al. (2010). Cluster observations of EMIC triggered emissions in association with Pc1 waves near Earth's plasmapause. *Geophysical Research Letters*, *37*, L09104. <https://doi.org/10.1029/2010GL042648>
- Reeves, G. D., McAdams, K. L., Friedel, R. H. W., & O'Brien, T. P. (2003). Acceleration and loss of relativistic electrons during geomagnetic storms. *Geophysical Research Letters*, *30*(10), 1529. <https://doi.org/10.1029/2002GL016513>
- Rodger, C. J., Clilverd, M. A., Green, J. C., & Lam, M. M. (2010). Use of POES SEM-2 observations to examine radiation belt dynamics and energetic electron precipitation into the atmosphere. *Journal of Geophysical Research: Space Physics*, *115*, A04202. <https://doi.org/10.1029/2008JA014023>
- Rodger, C. J., Hendry, A. T., Clilverd, M. A., Kletzing, C. A., Brundell, J. B., & Reeves, G. D. (2015). High-resolution in situ observations of electron precipitation causing EMIC waves. *Geophysical Research Letters*, *42*, 9633–9641. <https://doi.org/10.1002/2015GL066581>
- Saikin, A. A., Zhang, J.-C., Allen, R. C., Smith, C. W., Kistler, L. M., Spence, H. E., et al. (2015). The occurrence and wave properties of H^+ , He^+ , and O^+ -band EMIC waves observed by the Van Allen Probes. *Journal of Geophysical Research: Space Physics*, *120*, 7477–7492. <https://doi.org/10.1002/2015JA021358>
- Shprits, Y., Thorne, R., Friedel, R., Reeves, G., Fennell, J., Baker, D., & Kanekal, S. (2006). Outward radial diffusion driven by losses at magnetopause. *Journal of Geophysical Research*, *111*, A11214. <https://doi.org/10.1029/2006JA011657>
- Shprits, Y. Y., Kellerman, A., Aseev, N., Drozdov, A. Y., & Michaelis, I. (2017). Multi-MeV electron loss in the heart of the radiation belts. *Geophysical Research Letters*, *44*, 1204–1209. <https://doi.org/10.1002/2016GL072258>
- Spence, H. E., Reeves, G. D., Baker, D. N., Blake, J. B., Bolton, M., Bourdarie, S., et al. (2013). Science goals and overview of the Radiation Belt Storm Probes (RBSP) energetic particle, composition, and thermal plasma (ECT) suite on NASA's Van Allen Probes mission. *Space Science Reviews*, *179*(1–4), 311–336. <https://doi.org/10.1007/s11214-013-0007-5>
- Su, Z., Gao, Z., Zhu, H., Li, W., Zheng, H., Wang, Y., et al. (2016). Nonstorm time dropout of radiation belt electron fluxes on 24 September 2013. *Journal of Geophysical Research: Space Physics*, *121*, 6400–6416. <https://doi.org/10.1002/2016JA022546>
- Summers, D. (2005). Quasi-linear diffusion coefficients for field-aligned electromagnetic waves with applications to the magnetosphere. *Journal of Geophysical Research*, *110*, A08213. <https://doi.org/10.1029/2005JA011159>
- Summers, D., Shi, R., Engebretson, M. J., Oksavik, K., Manweiler, J. W., & Mitchell, D. G. (2017). Energetic proton spectra measured by the Van Allen probes. *Journal of Geophysical Research: Space Physics*, *122*, 10,129–10,144. <https://doi.org/10.1002/2017JA024484>
- Summers, D., & Thorne, R. M. (2003). Relativistic electron pitch-angle scattering by electromagnetic ion cyclotron waves during geomagnetic storms. *Journal of Geophysical Research*, *108*(A4), 1143. <https://doi.org/10.1029/2002JA009489>
- Summers, D., Thorne, R. M., & Xiao, F. (1998). Relativistic theory of wave-particle resonant diffusion with application to electron acceleration in the magnetosphere. *Journal of Geophysical Research*, *103*, 20,487–20,500. <https://doi.org/10.1029/98JA01740>
- Tetrick, S. S., Engebretson, M. J., Posch, J. L., Olson, C. N., Smith, C. W., Denton, R. E., et al. (2017). Location of intense electromagnetic ion cyclotron (EMIC) wave events relative to the plasmapause: Van Allen Probes observations. *Journal of Geophysical Research: Space Physics*, *122*, 4064–4088. <https://doi.org/10.1002/2016JA023392>
- Theodoridis, G. C., & Paolini, F. R. (1967). Pitch angle diffusion of relativistic outer belt electrons. *Annales Geophysicae*, *23*, 375.
- Thorne, R. M. (2010). Radiation belt dynamics: The importance of wave-particle interactions. *Geophysical Research Letters*, *37*, L22107. <https://doi.org/10.1029/2010GL044990>
- Tsyganenko, N. A., & Sitnov, M. I. (2005). Modeling the dynamics of the inner magnetosphere during strong geomagnetic storms. *Journal of Geophysical Research*, *110*, A03208. <https://doi.org/10.1029/2004JA010798>
- Turner, D. L., Claudepierre, S. G., Fennell, J. F., O'Brien, T. P., Blake, J. B., Lemon, C., et al. (2015). Energetic electron injections deep into the inner magnetosphere associated with substorm activity. *Geophysical Research Letters*, *42*, 2079–2087. <https://doi.org/10.1002/2015GL063225>
- Turner, D. L., Shprits, Y., Hartinger, M., & Angelopoulos, V. (2012). Explaining sudden losses of outer radiation belt electrons during geomagnetic storms. *Nature Physics*, *8*(3), 208–212. <https://doi.org/10.1038/nphys2185>
- Usanova, M. E., Drozdov, A., Orlova, K., Mann, I. R., Shprits, Y., Robertson, M. T., et al. (2014). Effect of EMIC waves on relativistic and ultrarelativistic electron populations: Ground-based and Van Allen Probes observations. *Geophysical Research Letters*, *41*, 1375–1381. <https://doi.org/10.1002/2013GL059024>
- Usanova, M. E., Mann, I. R., Rae, I. J., Kale, Z. C., Angelopoulos, V., Bonnell, J. W., et al. (2008). Multipoint observations of magnetospheric compression-related EMIC Pc1 waves by THEMIS and CARISMA. *Geophysical Research Letters*, *35*, L17525. <https://doi.org/10.1029/2008GL034458>
- Xiang, Z., Tu, W., Li, X., Ni, B., Morley, S. K., & Baker, D. N. (2017). Understanding the mechanisms of radiation belt dropouts observed by Van Allen Probes. *Journal of Geophysical Research: Space Physics*, *122*, 9858–9879. <https://doi.org/10.1002/2017JA024487>
- Xiao, F., Chen, L., He, Y., Su, Z., & Zheng, H. (2011). Modeling of precipitation loss of ring current protons by electromagnetic ion cyclotron waves. *Journal of Atmospheric and Solar-Terrestrial Physics*, *73*(1), 106–111. <https://doi.org/10.1016/j.jastp.2010.01.007>
- Yahnin, A. G., Yahnina, T. A., Raita, T., & Manninen, J. (2017). Ground pulsation magnetometer observations conjugated with relativistic electron precipitation. *Journal of Geophysical Research: Space Physics*, *122*, 9169–9182. <https://doi.org/10.1002/2017JA024249>
- Yahnin, A. G., Yahnina, T. A., Semenova, N. V., Gvozdevsky, B. B., & Pashin, A. B. (2016). Relativistic electron precipitation as seen by NOAA POES. *Journal of Geophysical Research: Space Physics*, *121*, 8286–8299. <https://doi.org/10.1002/2016JA022765>
- Yando, K., Millan, R. M., Green, J. C., & Evans, D. S. (2011). A Monte Carlo simulation of the NOAA POES r instrument. *Journal of Geophysical Research*, *116*, A10231. <https://doi.org/10.1029/2011JA016671>
- Yuan, Z., Deng, X., Lin, X., Pang, Y., Zhou, M., Décréau, P. M. E., et al. (2010). Link between EMIC waves in a plasmaspheric plume and a detached sub-auroral proton arc with observations of cluster and IMAGE satellites. *Geophysical Research Letters*, *37*, L07108. <https://doi.org/10.1029/2010GL042711>

- Zhang, J.-C., Kistler, L. M., Mouikis, C. G., Klecker, B., Sauvaud, J.-A., & Dunlop, M. W. (2011). A statistical study of EMIC wave-associated He⁺ energization in the outer magnetosphere: Cluster/CODIF observations. *Journal of Geophysics Research*, *116*, A11201. <https://doi.org/10.1029/2011JA016690>
- Zhang, X.-J., Li, W., Ma, Q., Thorne, R. M., Angelopoulos, V., Bortnik, J., et al. (2016). Direct evidence for EMIC wave scattering of relativistic electrons in space. *Journal of Geophysics Research: Space Physics*, *121*, 6620–6631. <https://doi.org/10.1002/2016JA022521>